Article

Visualization and Quantification of Drug Release by GSH-Responsive Multimodal Integrated Micelles

Long Xiao,[||] Lei Zhang,[||] Sha Li, Yue Zhu, Qiao Yu, Zhaoqing Liu, Maosong Qiu, Yu Li, Shizhen Chen,* and Xin Zhou*

Cite This: *JACS Au* 2024, 4, 1194−1206

Read Online

ACCESS | Metrics & More | Article Recommendations | Supporting Information

ABSTRACT: Using molecular imaging techniques to monitor biomarkers and drug release profiles simultaneously is highly advantageous for cancer diagnosis and treatment. However, achieving the accurate quantification of both biomarkers and drug release with a single imaging modality is challenging. This study presents the development of a glutathione (GSH)-responsive polymer-based micelle, PEG-SS-FCy7/PEG-SS-GEM (PSFG), which can precisely localize the tumor using bimodal imaging and prevent drug leakage. These PSFG micelles exhibit a small particle size of 106.3 ± 12.7 nm with a uniform size distribution, and the drug loading efficiency can also be easily controlled by

changing the PEG-SS-FCy7 (PSF) and PEG-SS-GEM (PSG) feeding ratio. The PSFG micelles display weak fluorescence emission and minimal drug release under physiological conditions but collapse in the presence of GSH to trigger near-infrared fluorescence and the ^{19}F magnetic resonance imaging signal, allowing for real-time monitoring of intracellular GSH levels and drug release. GSH could synergistically promote the disassembly of the micellar structure, resulting in accelerated probe and drug release of up to about 93.1% after 24 h. These prodrug micelles exhibit high *in vitro* and *in vivo* antitumor abilities with minimal side effects. The GSH-responsive drug delivery system with dual-modal imaging capability provides a promising imaging-guided chemotherapeutic platform to probe the tumor microenvironment and quantify real-time drug release profiles with minimal side effects.

KEYWORDS: glutathione, micelle, bimodal imaging, chemotherapy, lung cancer
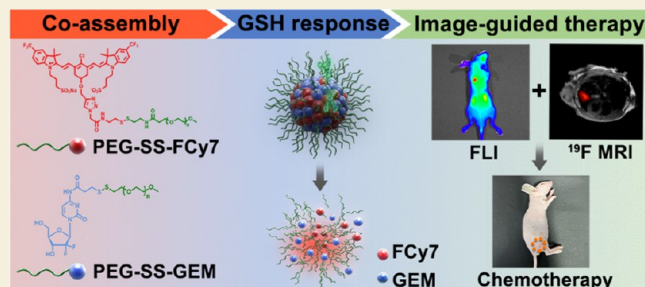
INTRODUCTION

In recent decades, cancer has remained one of the most lethal diseases in humans.[1] Conventional treatments like chemotherapy,[2] surgery,[3] and radiotherapy,[4] though widely used, often suffer from limited efficacy and severe side effects.[5] Thus, there is an urgent need to develop therapeutic strategies that are highly effective with minimal adverse effects. One promising avenue is using polymeric prodrug micelles with particle sizes below 200 nm, which can exploit the enhanced permeability and retention (EPR) effect to accumulate in tumor tissues.[6,7] A considerable number of prodrug nanocarriers with potent antitumor activity have been developed over the past few years.[8]

To ensure controlled drug release, stimulus-responsive polymeric micelle drug delivery systems have been investigated. These systems offer enhanced stability in normal tissues and rapid drug release in tumor microenvironments.[9−12] Polymeric prodrug micelles containing chemotherapeutic drugs linked with cleavable chemical bonds prevent drug leakage during circulation and respond to stimuli at the tumor site, triggering drug release.[13−24] Notably, GSH is crucial in maintaining intracellular redox balance and is associated with various diseases.[25−29] Hence, selective

detection and quantification of GSH hold valuable information for disease prognosis.[30] Several GSH-responsive drug release systems have been rationally designed for cancer treatment due to the significant difference between intracellular and extracellular GSH concentrations, and tumor cells contain a higher concentration of GSH, which is 4−7 times that of normal cells.[31]

However, conventional prodrug nanocarriers lack imaging capability, making it challenging to track their biodistribution or locate tumor sites accurately. To address this, prodrug nanocarriers with stimuli-responsive fluorescent probes, like those exhibiting aggregation-induced emission (AIE) or aggregation-induced quenching (ACQ) properties, have attracted significant attention.[32−36] Moreover, magnetic resonance imaging (MRI) is widely used in medical imaging due to its noninvasiveness, high penetration depth, and
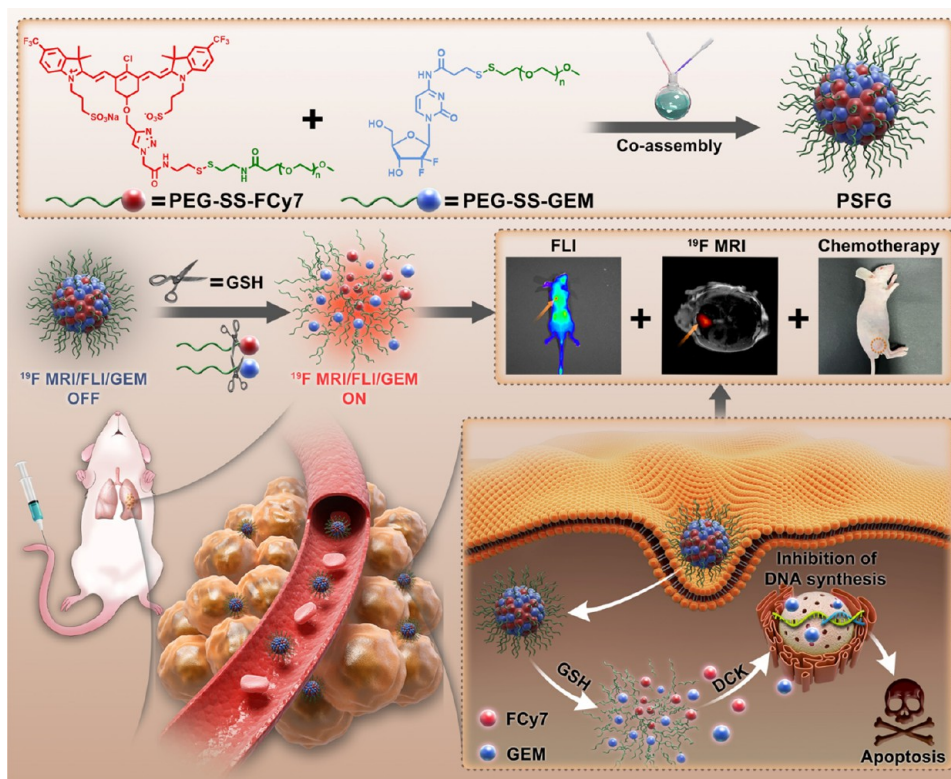
Scheme 1. Schematic Illustration of Coassembled PSFG Micelle and GSH Dual-Responsive Drug Release and Bioimaging[a]

[a]The co-assembly of two independent polymers into PSFG micelles results in a "turn off" of the fluorescence and ^{19}F MR signals. Once taken up by tumor cells, PSFG micelles are disintegrated by highly expressed GSH in the cytoplasm. When FCy7 and GEM are released, the "OFF" to "ON" changes in the fluorescence, and ^{19}F nuclear magnetic resonance (NMR)/MRI signals can not only reflect the content of GSH in tumor cells but also visualize the process of GEM release. GEM is phosphorylated by the action of deoxycytidine kinase (DCK), which inhibits DNA synthesis and induces apoptosis.

absence of harmful ionizing radiation.[37,38] Conventional ^{1}H MRI provides anatomical images of soft tissues using contrast agents.[39,40] As a complement to ^{1}H MRI, ^{19}F MRI selectively and quantitatively detects exogenous fluorinated probes without background interference.[41−43] As a result, ^{19}F MRI offers quantitative "hot-spot" images of targeted tissues through anatomical localization provided by ^{1}H MRI.[44,45]

Several analytical techniques have been utilized to detect GSH.[46−51] However, these methods have the same problem of detecting only low concentrations of GSH. Integrating ^{19}F MRI and fluorescence imaging into activatable nanoprobes will significantly expand the detection range of GSH from μM to mM. Integrating fluorescence and ^{19}F MR dual-imaging into stimuli-responsive nanoprobes provides real-time information about dynamic processes, enabling more accurate diagnosis and therapy.

In this study, GSH-responsive PSF and PSG coassembled PSFG prodrug micelles were designed for tumor bioimaging and therapy (Scheme 1). These micelles are uniform in size and stable under physiological conditions but rapidly disassembles upon GSH triggering. The GSH-induced dissociation of PSFG micelles results in a "switch-on" behavior of near-infrared (NIR) fluorescence and ^{19}F MRI for *in vivo* tumor imaging. Simultaneously, it accelerates drug release, demonstrating excellent antitumor efficacy with minimal side effects. Furthermore, this dual-modal imaging enables the simultaneous monitoring of intracellular GSH levels and drug release behavior, providing a powerful tool to probe the tumor

microenvironment and quantify real-time drug release. As a result, this approach shows great promise as an imaging-guided chemotherapeutic platform.

RESULTS AND DISCUSSION

Design, Synthesis, and Characterization of PSFG Micelles

An amphipathic probe called PSF, which is GSH-responsive and capable of bimodal imaging, has been rationally designed. This probe is created by conjugating the hydrophobic fluorinated Cy7 dye (FCy7) with the hydrophilic poly-(ethylene glycol) (PEG) chain through a disulfide bond (Figure S1). FCy7 was chosen as the NIR fluorescence probe due to its favorable properties, such as a high extinction coefficient, suitable emission wavelength, and excellent photo-chemical and photophysical stability, similar to Cy7.[52] This amphipathic PSF is expected to self-assemble into micelles in water, leading to the ACQ of FCy7 fluorescence and a weak ^{19}F MR signal due to the short transverse relaxation time (T_2).

The core of the micelles provides an ideal site for loading hydrophobic drugs. However, controlling encapsulation efficiency and achieving sustained release can be challenging.[53] To address this, a similar strategy was utilized by conjugating the antitumor drug gemcitabine (GEM) with PEG through disulfide bonds to create an amphiphilic polymer, which could easily coassemble with PSF to form a prodrug-integrated micelle (PSFG, Figure S1). Upon endocytosis in tumor cells, the disulfide bonds in PSFG are cleaved by elevated GSH levels in the cytoplasm. This triggers the release of FCy7 for
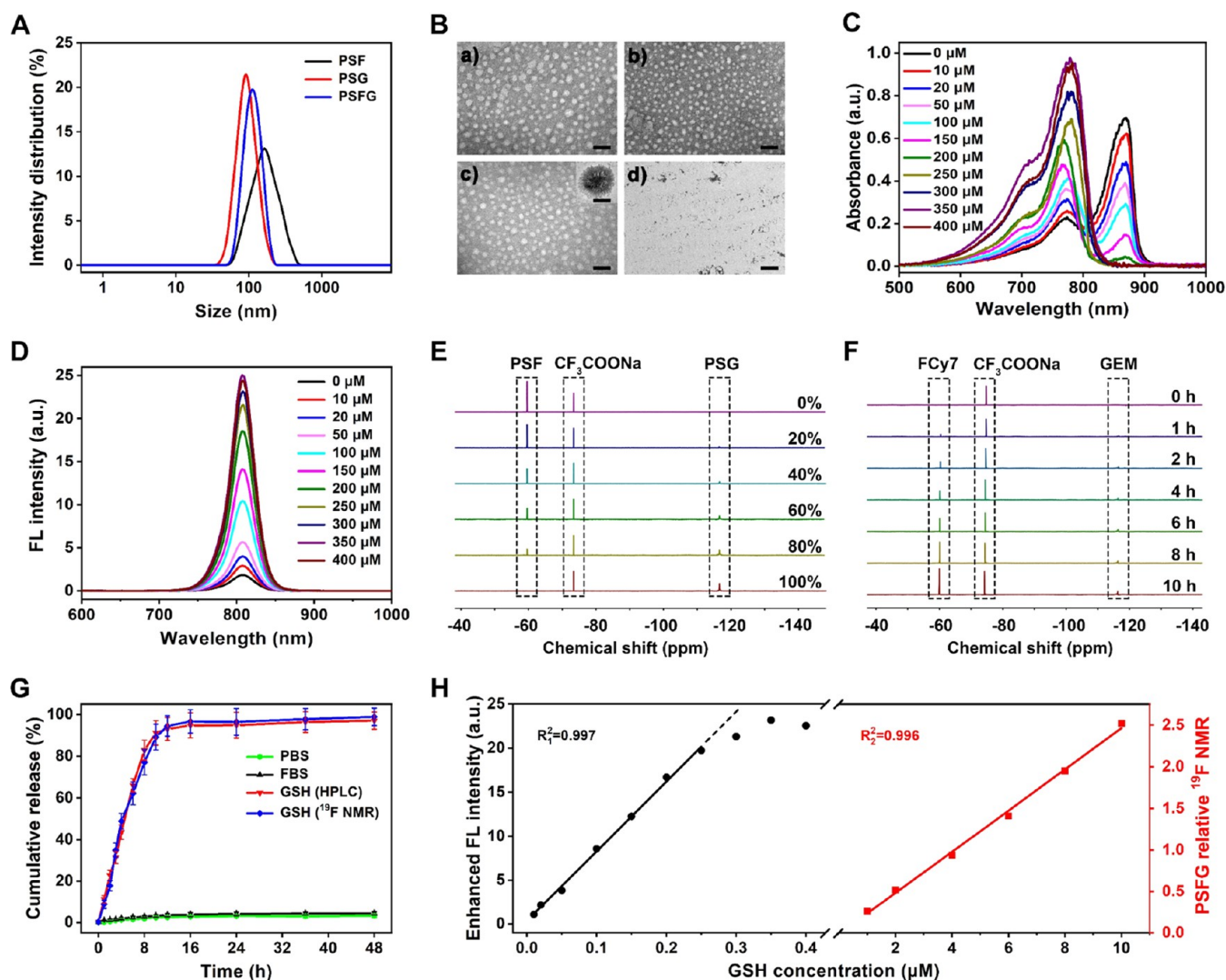
Figure 1. Characterization of PSFG properties and bimodal signal changes after the reaction with GSH. (A) Particle sizes of different polymeric micelles. (B) TEM images of (a) PSF, (b) PSG, (c) PSFG micelles in deionized water, and (d) PSFG micelles disassembled with GSH. Scale bars in (a)−(d) = 200 nm. Inset in (c): HR-TEM image of PSFG, scale bar = 50 nm. GSH concentration-dependent (C) absorption spectra and (D) fluorescence spectra of PSFG in PBS (10 mM, pH 7.4) after 10 h at 37 °C with λ_{ex} = 776 nm. (E) Concentration-dependent ^{19}F NMR spectra of PSFG with the mass fractions of PSG components in the entire PSFG micelle (0, 20, 40, 60, 80, and 100%). 50% DMSO + 40% H_2O+ 10% D_2O as solvent. CF_3COONa, with a peak of ^{19}F at −73.6 ppm, was used as an internal reference. (F) Time-dependent ^{19}F NMR spectra of PSFG (5 mg mL^{-1}) after the addition of GSH (10 mM) at 37 °C in PBS. (G) *In vitro* drug release of PSFG micelles in 10 mM GSH. The red and blue curves represent the GEM release results fitted by HPLC and ^{19}F NMR, respectively. (H) GSH concentration-dependent fluorescence intensity (black) at low GSH concentrations (≤0.25 mM) and GSH concentration-dependent ^{19}F NMR (red) at high GSH concentrations (1−10 mM). The black and red lines represent the linear fitting of the data.

tumor imaging and GEM for therapeutic purposes (Scheme 1). The synthesis and characterization of PSF and PSG are shown in the Supporting Information.

The coassembled PSFG micelles demonstrated a particle size of 106.3 ± 12.7 nm with a narrow size distribution of 0.196, as measured by dynamic light scattering (Figure 1A). Incorporating the hydrophobic GEM moiety into the core layer resulted in a smaller and more uniform hydrodynamic diameter for PSFG than that for PF and PSF (Table S1). The transmission electron microscopy (TEM) image displayed a smaller size with a homogeneous spherical outline of the PSFG micelle due to volume shrinkage after water evaporation (Figure 1B). Both characterization methods confirmed the successful formation of the micelle.

The measured ζ-potential of PSFG (phosphate-buffered saline (PBS), pH = 7.4) was −20.37 mV (Table S1), making it suitable for prolonged blood circulation. Additionally, PSFG demonstrated long-term stability in biological media, showing no signs of aggregation in water, PBS, fetal bovine serum (FBS), or F12K. Even after 14 days of incubation, the average hydrodynamic diameter of PSFG remained nearly unchanged, confirming its high stability (Figure S2). Overall, the stable PSFG micelle with a hydrophobic core and a PEGylated surface is expected to exhibit excellent biocompatibility, extended blood circulation, and controlled drug release during circulation.[54]

Fluorescence and ^{19}F NMR Signal Activation/Amplification of Multifunctional Self-Assembled PSFG Micelles

The dual-modal imaging agent PSF comprises a ^{19}F-bearing fluorescent group connected to PEG through a disulfide bond, which is susceptible to cleavage by reductive thiols. In this study, the negative control probe, PEG-FCy7 (PF), features a reduction-insensitive carbon−carbon bond, replacing the disulfide bond (Figure S3). This substitution is anticipated to hinder PF dissociation in the presence of thiols. The morphology and hydrodynamic diameter of the PF closely resemble those of PSF (Table S1). The amphiphilic polymer PSF was mixed with PSG in water to form the PSFG micelle. Compared to free FCy7 in water, the PSFG micelle showed a new red-shifted absorbance peak and attenuated fluorescence (Figure S4), which might be owing to the aggregation of FCy7 in the cores of the PSFG micelle.[55] These results indicated that the amphiphilic PSFG could self-assemble into micelles in an aqueous solution, probably via hydrophobic interactions and π−π stacking. The solvent-dependent fluorescence spectra of the micelle showed a gradual decrease in fluorescence intensity with an increase of the water fraction. This was accompanied by a decreased absorption peak at 776 nm and an increased absorption peak at 870 nm, suggesting that aggregation of the hydrophobic segment led to the ACQ of FCy7 fluorescence (Figure S5). The fluorescence-activatable micelles could help maximize the signal from the tissue of interest and minimize background signals, improving the sensitivity and specificity for subsequent *in vitro* and *in vivo* studies.

To confirm the activatable behavior of the PSFG micelle, its GSH-responsive fluorescence was then investigated. Upon incubation under physiological conditions (PBS buffer, pH 7.4, 37 °C), the PSFG micelle showed a new red-shifted absorbance peak at 870 nm without fluorescence emission and weak fluorescence emission at 808 nm (excited at 776 nm) in the absence of GSH, while its absorption at 776 nm and emission at 808 nm were much stronger when exposed to GSH (Figure 1C,D). In addition, the fluorescence intensity was positively dependent on the concentration of GSH, suggesting that its fluorescence was turned on by GSH in the system. After incubation with 350 μM GSH for 10 h, a maximum enhancement of about 17-fold in fluorescence intensity was achieved for the PSFG micelle. Furthermore, the fluorescence intensity of PSFG was linearly correlated with GSH concentration in the range of 5−250 μM, which may offer a convenient strategy to quantify GSH in cells (Figure S6). To further validate that the enhanced fluorescence signal in the solution was due to the free release of assembled micelles, fluorescence intensity tests using different concentrations of PSF in an aqueous solution were conducted. Below the critical micelle concentration (CMC), the fluorescence intensity of the solution increased linearly with increasing PSF concentration (Figure S7). Moreover, the fluorescence intensity remained nearly unchanged upon the addition of GSH, indicating that PSF was in a free state. However, when the concentration of PSF exceeded the CMC, micelles were formed in the solution, leading to an increased local concentration of the probe in the core of the micelle. Consequently, the solution's fluorescence decreased due to the ACQ effect. Upon addition of GSH, the release of micellar components resulted in an overall increase in the fluorescence intensity of the solution. Subsequently, the new product was characterized as FCy7-SH through ^{1}H NMR, high-performance liquid chromatography (HPLC), and high-resolution mass spectrometry (Figures S8−S11). The higher

polarity of FCy7-SH compared with the hydrophobic part of the micelle favors its release from the micellar core (Figures S12 and S13). These findings provide additional evidence for the effective cleavage of disulfide bonds within the micelles.

To evaluate the specificity of PSFG toward GSH, incubation experiments were conducted with PSFG, testing against various potential interference substances including KCl, CaCl$_2$, MgCl$_2$, glucose, bovine serum albumin (BSA), human serum albumin (HSA), vitamin C, FBS, Cys, and Hcy. Remarkably, only Cys-, HCy-, and GSH-treated PSFG exhibited an increased fluorescence intensity, with GSH producing the most pronounced effect (Figure S14). These results affirm that the reductive-responsive fluorescence of PSFG is specifically triggered in a reductive environment, positioning PSFG as a potential fluorescent probe within cancer cells.

The coassembled micelles, including PSF and PSG, were prepared in different proportions to achieve varying drug loadings, which could be measured precisely by ^{19}F NMR (Figure 1E). Next, the ^{19}F NMR signal changes in PSFG micelles upon incubation with GSH were investigated. Initially, the ^{19}F NMR signal of PSFG was "quenched" due to aggregation, which restricted the mobility of fluorine atoms, leading to an unmeasurably shortened transverse relaxation time (T_2) (Figure 1F). However, upon incubation with 10 mM GSH, a gradual increase in the ^{19}F NMR peak at −60.1 ppm was observed, with a time-dependent increase in the signal-to-noise ratio (SNR) of up to 63-fold at 10 h post-treatment. Additionally, the increased T_2 value of fluorine atoms (T_2 = 251.3 ms) indicated the cleavage of disulfide bonds, resulting in a less compact structure of the PSFG micelle and improved spin−spin relaxation and mobility restriction. This demonstrated a remarkable recovery of the T2 and ^{19}F NMR signal intensities.

This study used a PSF-to-PSG feeding ratio of 1:1 to balance imaging and treatment effects. Since both micellar segments were connected by disulfide bonds and comprised hydrophilic and hydrophobic parts, their sensitivity to the GSH response should be comparable. Hence, FCy7 cleaved from PSF could be positively related to drug release from PSG. Real-time GEM release could be monitored using ^{19}F NMR spectroscopy. The drug loading content (DLC) of PSFG was measured to be 21.2% through the ^{19}F NMR spectrum, which was consistent with the HPLC results. Without GSH, only 3.18% of the GEM was released after 24 h of incubation in PBS at 37 °C. However, in the presence of 10 mM GSH, approximately 93.1% GEM was released (Figures 1G and S15). The highly sensitive GSH-responsive behavior of these prodrug micelles highlights their suitability for tumor-targeted drug release.

Hence, it could be concluded that the bimodal probes showed a much broader linear range of GSH, which could be used for quantification in comparison to their single-modal counterparts. GSH can be quantified at low concentrations (5−250 μM) by fluorescence and at high concentrations (1−10 mM) by ^{19}F NMR, which are suitable for GSH detection in normal cells and tumor cells, respectively (Figures 1H and S16). Besides, GEM release can also be detected by the ^{19}F NMR method (Figure S16). These data collectively support the application of PSFG for *in vivo* tumor imaging and therapeutic purposes.
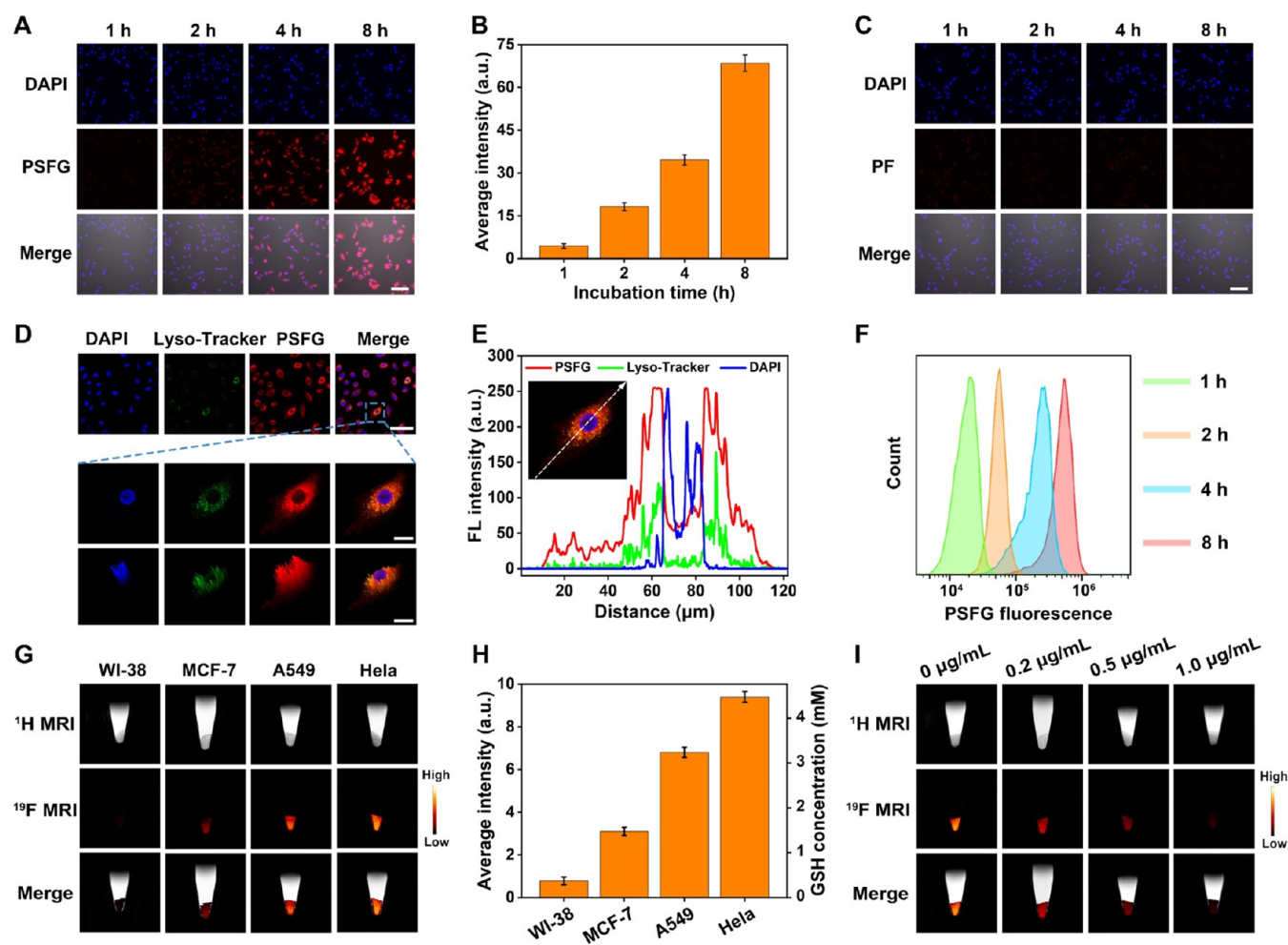
Figure 2. *In vitro* imaging of the PSFG micelle activity in tumor cells. Confocal laser scanning microscopy (CLSM) imaging of A549 cells incubated with PSFG micelles (100 μg mL^{-1}) (A) at different time points (1, 2, 4, and 8 h) and (B) corresponding fluorescence intensity; scale bar = 100 μm. (C) GSH-insensitive PF micelles (100 μg mL^{-1}) served as a control. The fluorescence images were collected in the NIR channel (λ_{em} = 808 ± 30 nm, λ_{ex} = 776 nm, CW laser). Scale bar = 100 μm. (D) CLSM image of A549 cells cocultured with PSFG micelles; scale bar = 50 μm. The scale bars for local magnification are 10 μm. (E) The signal intensity distribution of PSFG (red), Lyso-Tracker (green), and DAPI (blue) channels after treatment with PSFG micelles for 8 h. (F) Fluorescence intensity of intracellular PSFG at 1 h (green), 2 h (orange), 4 h (blue), and 8 h (red) after incubation by flow cytometry analysis. (G) ^{19}F MR phantom images of A549 cells incubated with PSFG micelles (1 mg mL^{-1}) with four cell lines (WI-38, MCF-7, A549, and HeLa) and (H) corresponding ^{19}F MRI signal intensities. (I) PEITC is involved in GSH consumption as a competitive inhibitor.

In Vitro GSH Imaging in Cancer Cells with Signal Activation/Amplification

The signal activation/amplification of the PSFG micelle under reductive conditions was investigated using A549 cells with elevated intracellular GSH levels as model cancer cells (Figure S17). Compared to A549 cells incubated with PF alone, the fluorescence intensity of the cells was enhanced 14.8-fold after treatment with PSFG (Figure S18). Micro-observation in a 6-well plate with PSFG- or PF-treated A549 cells revealed a strong red fluorescence signal inside the cells after 12 h, while cells treated with PF showed very weak intracellular fluorescence intensity (Figure 2A−C). Signal enhancement was only observed when the disulfide bonds were cleaved in the presence of GSH, leading to the release of FCy7 and GEM from the hydrophobic core, and triggering the corresponding signal activation/amplification. Both the red fluorescence of PSFG and the green fluorescence of the lysosome tracker were observed in the cytoplasm, with overlapping signals after 4 h of incubation, indicating that the PSFG micelles were internalized

into the cells via the endocytosis pathway. However, the higher intensity of the red fluorescence signals from PSFG, distinguished from the green signals, suggested that the micelles efficiently escaped from the lysosome (Figure 2D,E). Flow cytometry analysis further confirmed that fluorescence was 47-fold stronger at 8 h than at 1 h (Figure 2F). This GSH-activated PSFG fluorescence is advantageous for monitoring the disintegration and visualization of GSH *in vitro*.

Subsequently, the cellular uptake of PSFG micelles was investigated by using ^{19}F MRI. Four different cell lines, including one normal cell line and three cancer cell lines, were selected to determine GSH concentrations with ^{19}F MRI (Figure 2G). As expected, normal WI-38 cells with minimal cytoplasmic GSH levels showed the lowest ^{19}F MRI signal, while the signals in the three cancer cell lines strongly depended on their intracellular GSH levels without considering the factors of different cell lines with different uptake rates for micelles (Figure 2H). By plotting the ^{19}F MRI signals against the GSH concentration and back-calculating, the GSH content
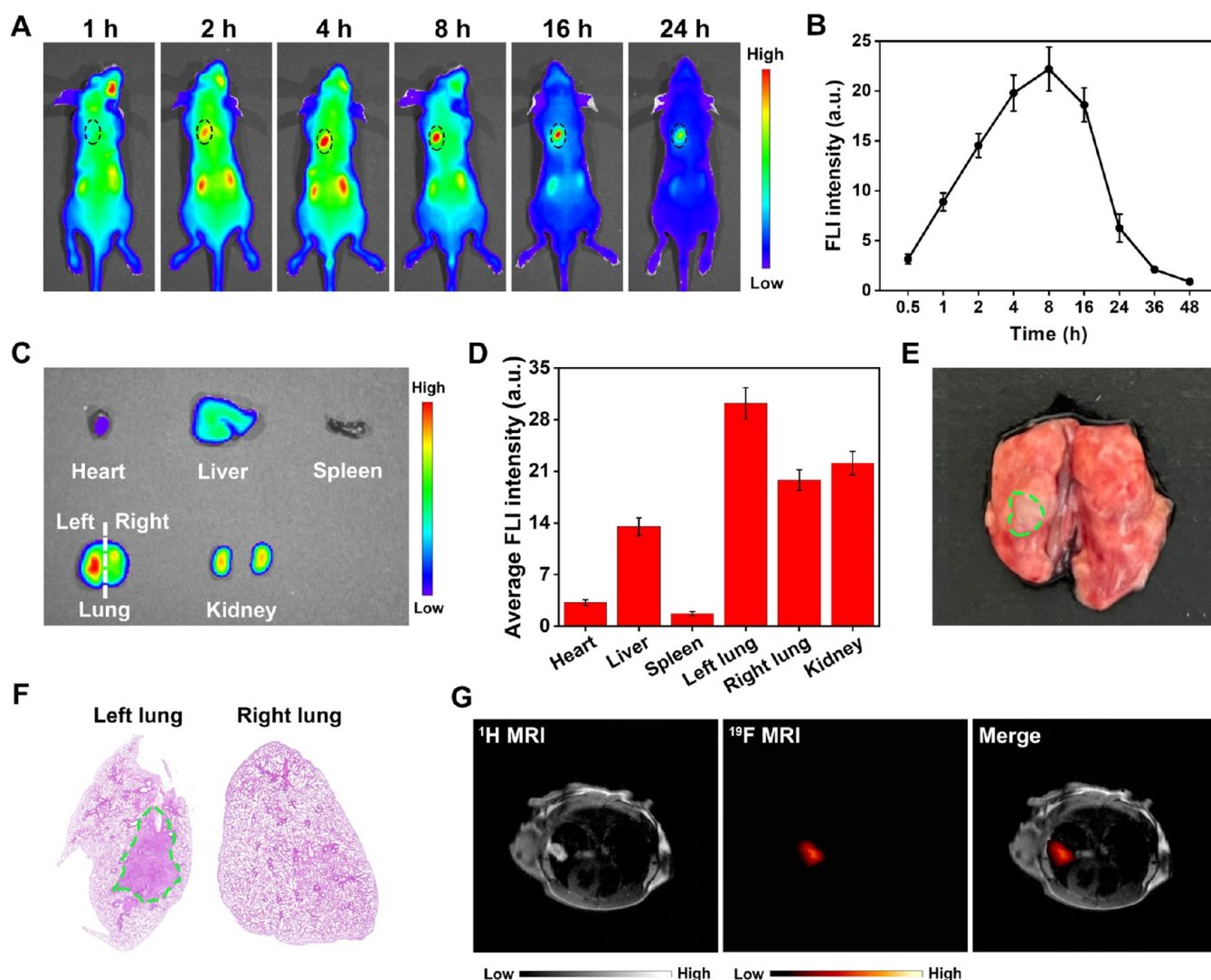
Figure 3. *In vivo* bioimaging of PSFG micelles after intravenous injection in *in situ* lung cancer-bearing mice. (A) Real-time biodistribution images were taken at predominant time points after post-PSFG administration. Black dashed circles are located at the tumor site. (B) Quantitative analysis of the *in vivo* fluorescence intensity of tumor sites circled on the left. (C) *Ex vivo* fluorescence images of the major organs and tumors 48 h postinjection of PSFG. (D) The quantitative analysis of fluorescence intensity in tumors or organs, with representative images and results expressed as the mean ± SD (n = 3 mice per group). (E) Photograph and (F) H&E staining of the lungs. The green dotted line indicates the tumor area. (G) *In vivo* ^{19}F MRI of an orthotopic lung cancer mouse model after drip irrigation of PSFG micelles (50 μL, 10 mg mL^{-1}, normal saline). The content of the target product (FCy7) was detected at −59.7 ppm.

in A549 cells was estimated to be approximately 3.24 mM. To verify that the disintegration of PSFG was attributable to GSH participation, cells were subjected to phenyl isothiocyanate (PEITC) treatment to reduce intracellular GSH levels in cancer cells. This intervention resulted in a significant reduction in the level of signals, as depicted in Figure 2I. These findings substantiate that the disassembly of PSFG occurs in response to GSH participation.

Validation of Synchronized Multiresponsive PSFG Micelles for Tumor Diagnosis *In Vivo*

Nanoparticles within the 50−200 nm size range have been reported to naturally accumulate at tumor sites through the EPR effect. To monitor the fate of post-intravenous PSFG injection, *in vivo* NIR fluorescence imaging analysis was conducted on lung cancer-afflicted mice using an IVIS Imaging System, with a control group of mice treated with saline. Fluorescence images of the mice were captured at various time intervals postinjection. Mice treated with PF exhibited

nonspecific fluorescence dispersed throughout their bodies (Figure S19). In contrast, mice treated with PSFG displayed a robust fluorescence signal specifically localized in the left lung area, where the tumor was situated (Figure 3A). The fluorescence signal at the tumor site peaked 8 h postinjection and gradually diminished over time (Figure 3B). Notably, the average fluorescence signals in the left lung surpassed those in the right lung and other organs, indicating distinct tumor-targeting properties (Figure 3C, D). The *ex vivo* fluorescence signal of the left lung aligned well with *in vivo* observations, showcasing the most intense fluorescence signal at the tumor sites in the left lung. This observation was corroborated by the lung hematoxylin and eosin (H&E) staining results, validating the enhancement of the lung fluorescence signal, specifically in the lung tumor area (Figure 3E,F). These collective findings underscore the potential of PSFG as a passive, targeted tumor fluorescence imaging agent. Next, the GSH-responsive "turning on" of the ^{19}F signal was investigated *in situ* in lung tumor mice
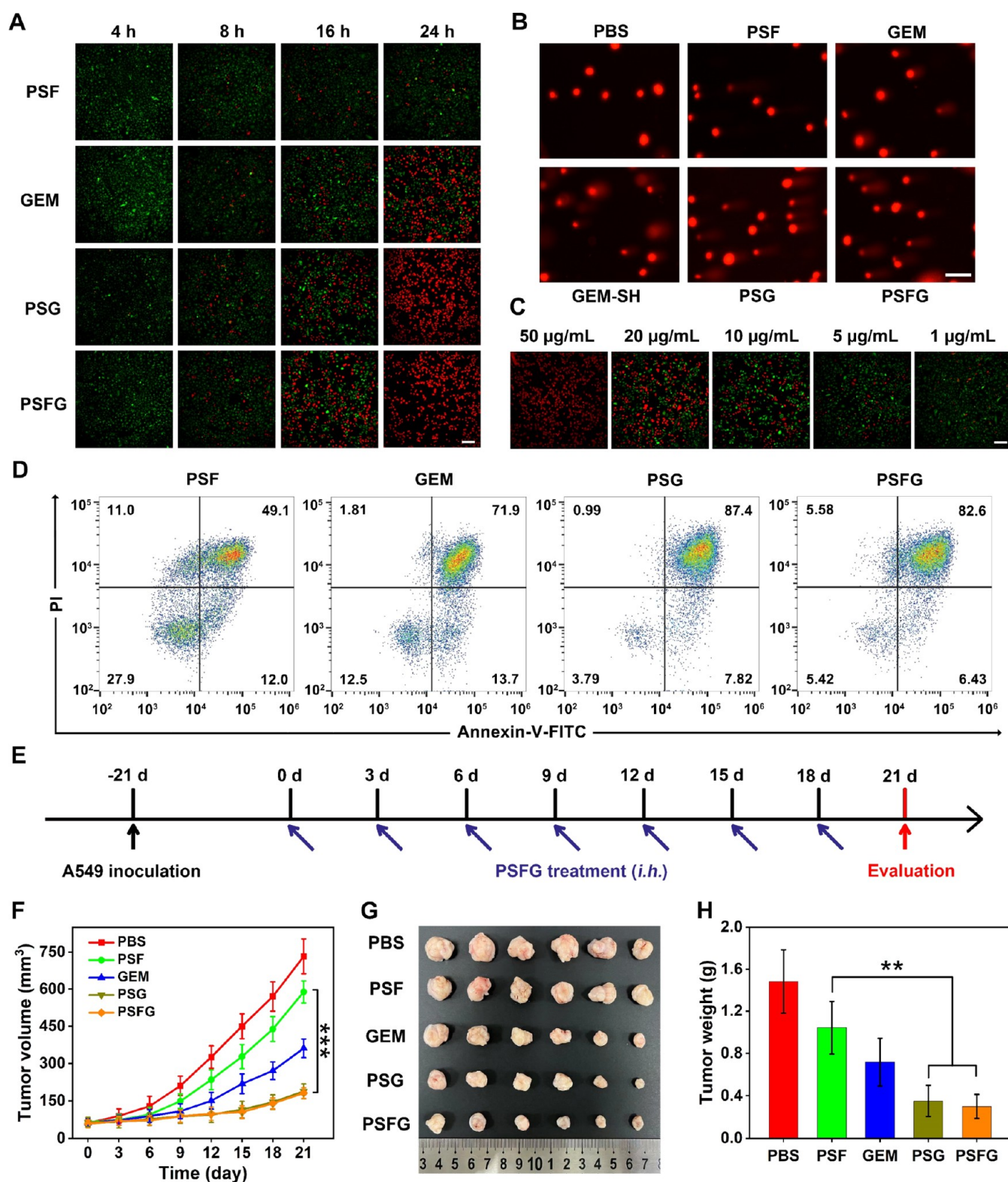
Figure 4. *In vitro* and *in vivo* antitumor effects of PSFG micelles after incubation with A549 cells or subcutaneous injection in male Balb/c nude mice bearing A549 xenografts. (A) Representative images of live (green) and dead (red) assays of A549 cells treated with PSF, GEM, PSG, and PSFG with the same GEM content. Scale bar = 200 μm. (B) Deoxyribonucleic acid (DNA) damage in A549 cells was detected by comet electrophoresis (single-cell gel electrophoresis experiment). Scale bar = 20 μm. (C) Representative images of live (green) and dead (red) assay of A549 cells treated with different PSFG concentrations. Scale bar = 200 μm. (D) Assessment of Cell death mechanism with annexin-V-FITC/PI by flow cytometry. (E) Timeline of the administration of PSFG micelles and control groups to A549 tumors. (F) *In vivo* antitumor study of PBS, PSF, free GEM, PSG, and PSFG. The variation of tumor volume changes over 21 days after injection. The drugs injected in the three experimental groups in GEM, PSG, and PSFG were measured at the same GEM equivalence (mean $\pm$ SD, $n = 6$, ***$p < 0.001$). (G) Photographs and (H) weights of tumors after treatment in different groups for 21 days (mean $\pm$ SD, $n = 6$, **$p < 0.01$).
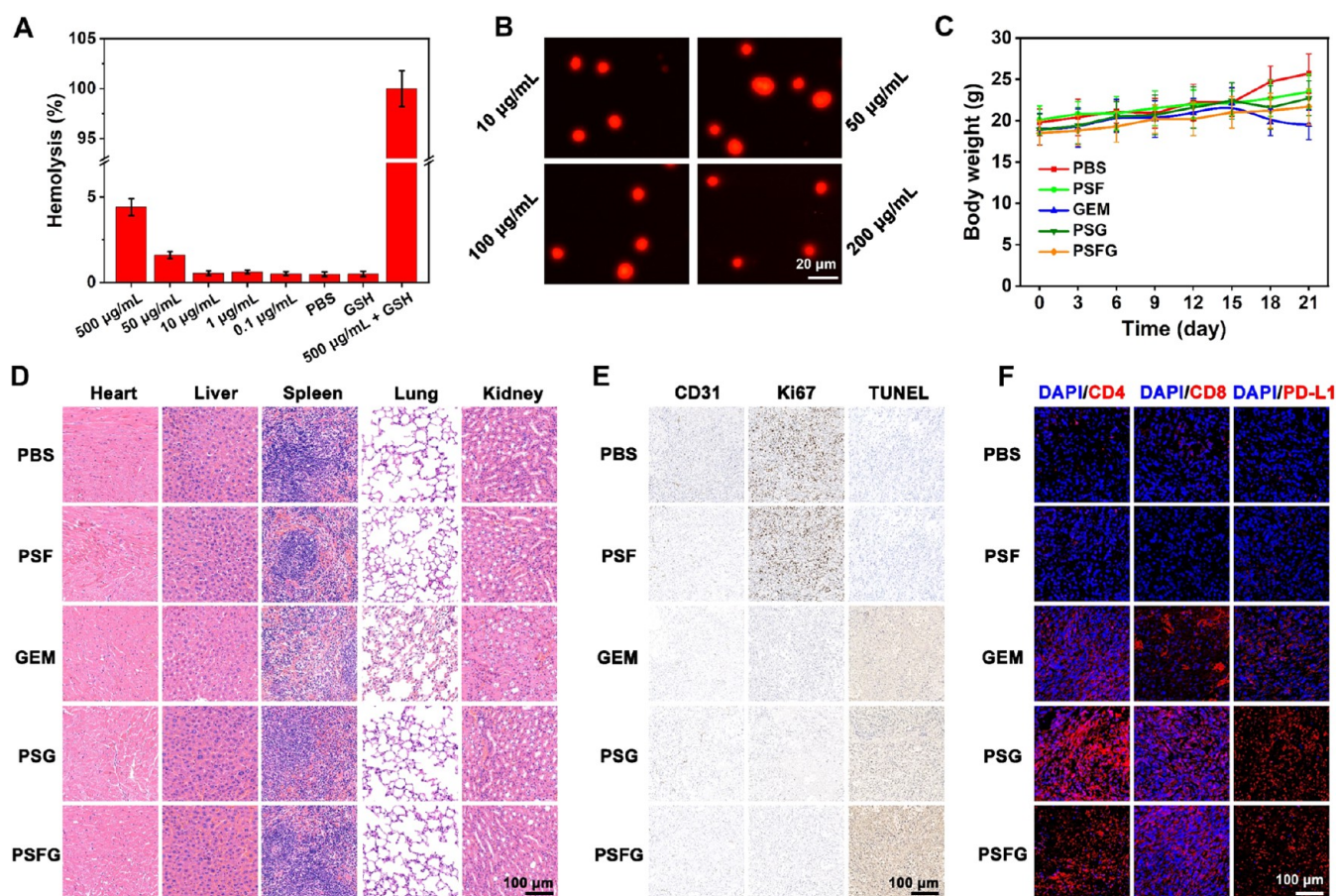
Figure 5. Safety evaluation of different groups of male Balb/c nude mice bearing the A549 xenograft model. (A) In the hemolysis analysis of micelles at different concentrations, the percent of hemolysis was less than 5%, even at micellar concentrations up to 500 μg mL^{-1}. (B) Damage to normal cellular DNA by PSFG was detected by comet electrophoresis. Scale bar = 20 μm. (C) Body weight changes over 21 days after the injection. (D) Images of H&E assays for the heart, liver, spleen, lungs, kidneys, and tumors after treatment with PBS, PSF, free GEM, PSG, and PSFG micelles over 21 days. Scale bar = 100 μm. (E) Immunohistochemical (IHC) analysis of tumor sections (CD31, Ki67, and TUNEL). Scale bar = 100 μm. (F) Immunofluorescence images of tumor tissues stained for CD4$^+$, CD8$^+$, and PD-L1 on day 21 (n = 7, all tissues: 100×). Scale bar = 100 μm.

using PSFG micelles administered via nasal drip irrigation at a dosage of 50 μL (10 mg mL^{-1}) PSFG. ^{19}F MR imaging was performed 2 h postinjection of PSFG micelles, and the signal was significantly enhanced and reduced with time after irrigation with micelles (Figures 3G and S20). These results demonstrate the high specificity and sensitivity of ^{19}F MRI using PSFG as a multiresponsive probe. Moreover, enhanced ^{19}F MRI signals at the tumor site hold promise for accurate and sensitive tumor diagnosis through imaging.

In Vivo Antitumor Efficacy

Before *in vivo* antitumor application, cell viability was evaluated in A549 cells. Different concentrations of the corresponding micelles (PF, PSF, and PSFG) ranging from 20 to 100 μg mL^{-1} were added to A549 cells for the MTT assay. The cell viability of the control group (PF) at each concentration was above 90%, indicating excellent biocompatibility of the blank micelles. Moreover, cellular MTT data from the PSF group confirmed that FCy7 also contributed to tumor cell suppression to some extent (Figure S21). Meanwhile, free GEM and GEM-loaded PSFG showed significant dose-dependent inhibition of A549 cells, with approximately 62.4 and 78.6% inhibition at a GEM concentration of 10 μg mL^{-1} (Figure S22). The high tumor cell inhibition ability made these

prodrug micelles suitable for *in vivo* antitumor applications due to their superior water solubility compared to free GEM. Furthermore, a live/dead cell staining assay with calcein-AM/PI was performed to demonstrate the tumor cell-killing ability of PSFG. Consistent with the MTT assay results, PSFG showed the highest percentage of dead cells (red fluorescence) after 24 h (nearly 100%; Figures 4A and S23). The comet assay results also indicated that comet tails in tumor cells were significantly longer in the PSFG group than in the other groups (Figure 4B). Moreover, the series of PSFG concentrations used in the cell-killing experiments displayed a similar trend, even at a low concentration of 1 μg mL^{-1}, showing a considerable killing effect on A549 cells (Figure 4C). Furthermore, flow cytometry expounded the lethal mechanism of the PSFG micelle, suggesting an apoptosis-activated cell death pathway (Figures 4D and S24). These results conclusively demonstrated that PSFG micelles effectively delivered the drug into cells and activated its therapeutic action under the influence of GSH, thereby providing a solid foundation for *in vivo* treatment. The use of both fluorescence and ^{19}F NMR techniques to monitor drug release behavior *in vitro* was well-designed and executed. Rarely, *in vivo* implementation can be challenging due to the complexity of the body's metabolism.

Next, a xenograft A549 tumor model was established to test the effectiveness of the proposed activatable nanoprobes for *in vivo* tumor therapy. The mice were randomly assigned to five groups and subjected to different treatments (PBS, PSF, GEM, PSG, and PSFG) via subcutaneous injection (Figure 4E). Tumors in PBS-treated mice grew rapidly, with a 14-fold increase relative to the initial tumor volume on the last day of treatment. Free GEM treatment exhibited moderate antitumor efficacy. However, both PSG and PSFG demonstrated outstanding tumor inhibition efficacy. Particularly, PSFG administered via subcutaneous injection exhibited remarkable antitumor efficiency compared to free GEM after 21 days (Figure 4F). Interestingly, the PSF group also showed a specific antitumor effect compared to the PBS group, possibly due to the detached FCy7 with a particular lethality to tumor cells. After 21 days of treatment, the mice were sacrificed and the tumors were isolated, imaged, and weighed. The images and weights of the isolated tumors further confirmed that PSFG micelles had better antitumor efficiency than PSF and free GEM (Figure 4G,H). These results substantiated the key inhibitory role of the GEM component of PSFG in tumor therapy. Importantly, the half-life of free GEM in the blood is usually only a few minutes, which limits its enrichment and retention at the tumor site. In contrast, the PSFG micellar structure extended the circulation time in the blood, enabled tumor site enrichment by the EPR effect, and triggered the release of chemotherapy drugs in response to GSH. As a result, PSFG exhibited significantly improved therapeutic effects on tumors with enhanced biosafety compared to free GEM.

Biosafety Assessment and Immunocytochemistry Analysis

The hemolysis of polymeric micelles was evaluated to test biocompatibility, and it was found that less than 5% hemolysis was observed when exposed to micellar concentrations of up to 500 μg mL^{-1} (Figures 5A and S25). Detection by comet electrophoresis also confirmed that the damage to normal WI-38 cells by the PSFG micelles was almost negligible (Figure 5B). We also tracked the mice's body weight to evaluate any potential side effects. The body weight variation of the mice that received PSFG micelle treatment was similar to that of mice treated with PBS, indicating the satisfactory biosafety of PSFG micelles (Figure 5C). However, the mice subjected to free GEM dosing suffered remarkable body weight loss from day 18 *i.h.*, indicating potential adverse effects verified by the observations of H&E-stained tissues. In addition, acute toxicity of PSFG on day 7 *i.p.* was assessed, and no death was observed in the PSFG-treated group, indicating that the micelles did not result in the formation of pulmonary embolisms. The blood biochemistry of the mice exposed to PSFG and PBS was conducted to assess their systemic toxicity as well. All of the typical blood serum biochemical indices, including alanine aminotransferase (ALT), alkaline phosphatase (ALP), and aspartate aminotransferase (AST), of the mice exposed to PSFG were comparable to those of the control group (Table S2). All of these results collectively revealed that PSFG exhibited good short-term biocompatibility at the tested dosages.

After 21 days of treatment, all of the mice were sacrificed and dissected to isolate their major organs (heart, liver, spleen, lungs, and kidneys) and tumors. Tissue slides were then prepared for H&E staining to evaluate organ toxicity and antitumor efficacy of the different treatments. Notably, the free GEM-treated mice showed significant inflammation and focal necrosis in major organs (liver, spleen, and lung), while the PBS- and PSFG-treated groups were relatively normal (Figure 5D). In addition, visible tumor metastases were observed in the livers of the saline- and free GEM-treated groups. In contrast, they were rarely found in the micelle-treated group, suggesting that the PSFG micelle could potentially prevent tumor metastasis. In addition, more apoptosis was observed in the tumor sections of micelle-treated mice. Therefore, the PSFG micelle reduces the side effects of free GEMs and has satisfactory antitumor efficacy.

These results demonstrate the good biocompatibility of PSFG. Using PSFG as both a chemotherapeutic agent and a responsive fluorescence and ^{19}F MRI probe, it was expected that chemotherapy treatment could be monitored by fluorescence and ^{19}F MRI in real-time with a high signal-to-noise ratio, which is extremely important for tumor imaging, and it may even be feasible for image-guided cancer therapy in deep tissues *in vivo*. In addition, these results suggest that prodrug micelles could reduce the side effects of GEM on normal cells and organs.

To explore blood vessel angiogenesis, cell proliferation, and apoptosis at the tumor site following various treatments, we conducted staining for platelet endothelial cell adhesion molecule-1 (CD31), Ki67, and terminal deoxynucleotidyl transferase dUTP nick-end labeling (TUNEL). CD31 is a biomarker of tumor angiogenesis. As shown in Figure 5E, the tumor microvessel density of PSFG-treated mice was significantly reduced compared to that of saline- and PSF-treated mice, verifying its superior antitumor efficacy over the rest of the treatments. Ki67 is widely used as a proliferation marker in routine pathological investigations. Ki67 expression in saline- and PSF-treated mice was higher than that of PSFG- or PSG-treated mice, suggesting that PSFG was able to inhibit the proliferation of tumor cells better. TUNEL staining is a general method to detect DNA fragments from apoptotic cells. The TUNEL assay showed that mice treated with micelles had the highest apoptosis ratio, which indicated that these micelles induced the most apoptosis of the tumor cells. Considering the mechanism by which GEM activates the immune system, it was deduced that treating a subcutaneous tumor with PSFG could mediate the abscopal effect by boosting specific T-cell activation and infiltration. The results from immunofluorescence staining suggested that the frequency of CD4$^+$ T helper cells infiltrating the tumors in the PSFG group was significantly increased. Meanwhile, the cytotoxic CD8$^+$ T cells in the PSFG group remained at the highest level (Figure 5F). All these results suggested that PSFG micelles could significantly improve antitumor efficacy by inhibiting blood vessel angiogenesis and cell proliferation and inducing cell apoptosis, which should be attributed to their accumulation at tumor sites and the GSH-triggered drug release

■ CONCLUSIONS

In summary, we successfully developed a dual-modal contrast agent-mediated prodrug integrative micelle named PSFG, enabling the precise diagnosis of early-stage lung cancer *in vivo*. The synthesis of PSF nanoprobes and PSG nano prodrugs involved the conjugation of PEG with FCy7 and GEM derivatives through a disulfide linkage. The coassembled PSFG micelles displayed minimal fluorescence and ^{19}F NMR/MRI signals (OFF) under normal conditions. However, exposure to reduced conditions, such as the presence of GSH, triggered a remarkable turn-on effect, with a maximum fluorescence turn-

on ratio of approximately 17-fold and 63-fold enhancement in the ^{19}F NMR signal. The GSH-responsive PSFG-ACQ prodrug micelles were specifically designed to selectively release GEM at tumor sites while simultaneously imaging the tumor using GSH-triggered fluorescence and ^{19}F MRI. These prodrug micelles exhibited excellent GSH-responsive behavior, effectively preventing drug leakage into the bloodstream. Additionally, GSH synergistically induced disassembly and subsequent drug release from the micelles. The high hemocompatibility and cell-membrane-mimetic antifouling PEG shell ensured prolonged blood circulation of the micelles, facilitating their accumulation at tumor sites. Furthermore, these prodrug micelles demonstrated significant antitumor activity with minimal side effects in both *in vitro* and *in vivo* experiments. Consequently, these dual-responsive prodrug micelles represent a promising strategy for designing nanocarriers for drug delivery and bioimaging, thereby positioning them as potential candidates for cancer theranostics. Furthermore, the PSFG micelles showcased exceptional biocompatibility and exhibited no tissue toxicity *in vivo*. Thus, we posit that this straightforward system can be readily expanded for the sensitive and accurate sensing and imaging of other targets in the tumor microenvironment, such as reactive oxygen species, acidosis, and hypoxia. Combining high-sensitivity fluorescence imaging with high-contrast ^{19}F MRI to image tumors *in vivo* will allow us to obtain richer diagnostic information. Moreover, the signal activation/amplification strategy employed in creating this probe can serve as a valuable guide for designing more innovative probes to detect biological targets with high specificity and sensitivity. The versatility and potential applications of this approach hold promise for advancing cancer diagnosis and therapy in the future.

METHODS

Materials

Unless otherwise noted, all chemical reagents were purchased from commercial suppliers and used without further purification. The detailed synthesis route can be found in the Supporting Information.

Preparation of Co-assembly Polymeric Micelles

PSF (30 mg) and PSG (15 mg) were dissolved in 1 mL DMSO, followed by slow injection into vigorously stirred deionized water (10 mL). The mixture was stirred for 1 h. Subsequently, the resulting solution was transferred to a dialysis bag (MWCO = 1000) and dialyzed against deionized water for 2 days. Finally, the solution was filtered using a 220 nm filter membrane.

In Vitro Drug Release

The *in vitro* release of GEM from the PSFG micelle was evaluated by using dialysis methods. Briefly, 2 mL of the PSFG micelle solution was employed, and the GEM release was monitored through a dialysis bag (MWCO = 2000) immersed in 10 mL PBS solution (pH 7.4), both in the presence and absence of 10 mM GSH at 37 °C. At specific intervals, 1 mL of the release medium was sampled, and an equal volume was replenished to maintain a constant volume. The absorbance of GEM was measured at a wavelength of 268 nm, and GEM concentration was determined using a pre-established calibration curve. The results were graphically represented as the cumulative release (%) over time.

Cellular Uptake and Fluorescence Test Off/On

The cellular uptake of PSFG coassembly polymeric micelles was evaluated by confocal laser scanning microscopy (CLSM). The cells were seeded in 6-well plates at a density of 2×10^5 cells per well in 2 mL complete F12K media containing 10% fetal bovine serum, supplemented with 100 U/mL penicillin and 100 U/mL streptomycin, and incubated at 37 °C in 5% CO$_2$ atmosphere for 24 h. PSFG micelles in a medium with the same concentration of FCy (10 μg/mL) were added. After different time points, the plate was observed with an *in vivo* fluorescence imaging system or an Olympus U-HGLGPS fluorescence microscope with or without replacing the original medium. For a 6-well plate observed with a fluorescence microscope, 1 mM GSH, which could imitate the reduction environment, was added to each well for further observation. Then, the cells were washed with PBS, and 4% formaldehyde was added for 25 min of incubation. 4,6-Diamino-2-phenyl indole (DAPI, 5 μg/mL) was further used for nucleus staining (10 min). After washing with PBS, each well was observed with a fluorescence microscope for cellular uptake evaluation. To better compare the cell-uptake results, flow cytometry analysis was performed using a flow cytometer (Beckman), which collected 10,000 gated events for each sample.

In Vivo NIR Imaging Study

Before the imaging experiment, the *in situ* lung cancer mice were anesthetized using isoflurane. Subsequently, 100 μL of PSFG NPs (100 μg/mL) was administered through the posterior venous plexus. Fluorescence imaging was conducted using the PerkinElmer *in vivo* optical imaging system (IVIS) at intervals of 0.5, 1, 2, 4, 8, 12, 16, 24, 36, and 48 h postinjection, employing an excitation band-pass filter at 745 nm and emission at 810 nm.

In Vivo MRI Study

In vivo MR imaging was conducted on anesthetized mice using 150 μL of 1% pentobarbital sodium. The MRI procedure was performed on a 400 MHz MRI instrument (Bruker, Germany), employing a ^{1}H MRI technique with a RARE sequence (repetition time/echo time (TR/TE), 3000/40 ms; flip angle, 90°; field of view (FOV), 30 mm × 30 mm; acquisition matrix, 256 × 256; and slice thickness 1.0 mm). RF transmission and reception were facilitated by an ^{19}F (376.5 MHz) coil with a 10 mm inner diameter. Probes were imaged both in solution and cells using a ^{19}F MR imaging technique, with parameters set as follows: repetition time (TR) = 3000 ms, effective time (TE) = 3 ms, rare factor = 4, matrix size = 64 × 64, number of averages = 64, FOV = 37 mm × 37 mm, slice thickness (SI) = 10 mm, bandwidth = 5400 Hz, and a total scan time of approximately 30 min. The mice underwent scans before and after the intravenous injection of 50 μL saline solution containing 400 μg of PSFG nanoprobes at the 2-h mark.

Statistical Analysis

The quantitative data are expressed as the mean ± standard deviation unless otherwise stated. The Students' *t-test* was used to determine the statistical comparison between the two groups. $P^* < 0.05$ was considered statistically significant. All statistical calculations were performed using Origin Pro 8.5.

ASSOCIATED CONTENT

Supporting Information

The Supporting Information is available free of charge at https://pubs.acs.org/doi/10.1021/jacsau.4c00009.

Synthetic routes of PSF and PSG; NMR, MS, and HPLC of intermediates and products; particle size and potential energy of four different micelles; UV−vis absorption spectra and fluorescence emission spectra of PSFG and FCy7; HPLC profiles of PSFG mixed with GSH; fluorescence responses of PSFG to various substances; fluorescence observation of different treatments after incubation with A549 cells; observation of *in vivo* fluorescence and MRI in orthotopic lung cancer model mice; cytotoxicity of free GEM and PSFG (PDF)

■ AUTHOR INFORMATION

Corresponding Authors

Shizhen Chen − *State Key Laboratory of Magnetic Resonance and Atomic and Molecular Physics, National Center for Magnetic Resonance in Wuhan, Wuhan Institute of Physics and Mathematics, Innovation Academy for Precision Measurement Science and Technology, Chinese Academy of Sciences, Wuhan 430071, P. R. China; University of Chinese Academy of Sciences, Beijing 100049, P. R. China; School of Biomedical Engineering, Hainan University, Haikou, Hainan 570228, P. R. China;* Email: chenshizhen@wipm.ac.cn

Xin Zhou − *State Key Laboratory of Magnetic Resonance and Atomic and Molecular Physics, National Center for Magnetic Resonance in Wuhan, Wuhan Institute of Physics and Mathematics, Innovation Academy for Precision Measurement Science and Technology, Chinese Academy of Sciences, Wuhan 430071, P. R. China; University of Chinese Academy of Sciences, Beijing 100049, P. R. China; School of Biomedical Engineering, Hainan University, Haikou, Hainan 570228, P. R. China;* ⊙ orcid.org/0000-0002-5580-7907; Email: xinzhou@wipm.ac.cn

Authors

Long Xiao − *State Key Laboratory of Magnetic Resonance and Atomic and Molecular Physics, National Center for Magnetic Resonance in Wuhan, Wuhan Institute of Physics and Mathematics, Innovation Academy for Precision Measurement Science and Technology, Chinese Academy of Sciences, Wuhan 430071, P. R. China; University of Chinese Academy of Sciences, Beijing 100049, P. R. China*

Lei Zhang − *State Key Laboratory of Magnetic Resonance and Atomic and Molecular Physics, National Center for Magnetic Resonance in Wuhan, Wuhan Institute of Physics and Mathematics, Innovation Academy for Precision Measurement Science and Technology, Chinese Academy of Sciences, Wuhan 430071, P. R. China; University of Chinese Academy of Sciences, Beijing 100049, P. R. China*

Sha Li − *State Key Laboratory of Magnetic Resonance and Atomic and Molecular Physics, National Center for Magnetic Resonance in Wuhan, Wuhan Institute of Physics and Mathematics, Innovation Academy for Precision Measurement Science and Technology, Chinese Academy of Sciences, Wuhan 430071, P. R. China*

Yue Zhu − *State Key Laboratory of Magnetic Resonance and Atomic and Molecular Physics, National Center for Magnetic Resonance in Wuhan, Wuhan Institute of Physics and Mathematics, Innovation Academy for Precision Measurement Science and Technology, Chinese Academy of Sciences, Wuhan 430071, P. R. China*

Qiao Yu − *State Key Laboratory of Magnetic Resonance and Atomic and Molecular Physics, National Center for Magnetic Resonance in Wuhan, Wuhan Institute of Physics and Mathematics, Innovation Academy for Precision Measurement Science and Technology, Chinese Academy of Sciences, Wuhan 430071, P. R. China*

Zhaoqing Liu − *State Key Laboratory of Magnetic Resonance and Atomic and Molecular Physics, National Center for Magnetic Resonance in Wuhan, Wuhan Institute of Physics and Mathematics, Innovation Academy for Precision Measurement Science and Technology, Chinese Academy of Sciences, Wuhan 430071, P. R. China; University of Chinese Academy of Sciences, Beijing 100049, P. R. China*

Maosong Qiu − *State Key Laboratory of Magnetic Resonance and Atomic and Molecular Physics, National Center for Magnetic Resonance in Wuhan, Wuhan Institute of Physics and Mathematics, Innovation Academy for Precision Measurement Science and Technology, Chinese Academy of Sciences, Wuhan 430071, P. R. China; University of Chinese Academy of Sciences, Beijing 100049, P. R. China*

Yu Li − *State Key Laboratory of Magnetic Resonance and Atomic and Molecular Physics, National Center for Magnetic Resonance in Wuhan, Wuhan Institute of Physics and Mathematics, Innovation Academy for Precision Measurement Science and Technology, Chinese Academy of Sciences, Wuhan 430071, P. R. China; University of Chinese Academy of Sciences, Beijing 100049, P. R. China*

Complete contact information is available at:
https://pubs.acs.org/10.1021/jacsau.4c00009

Author Contributions

‖L.X. and L.Z. contributed equally to this work. L.X. and L.Z. conceived and performed the experimental work and wrote the first draft of the manuscript. S.L., Y.Z., Q.Y., and Z.L. carried out practical work and discussed the results. M.Q. and Y.L. planned and designed the experiments. S.C. and X.Z. supervised the work, discussed experiments and results, and wrote the final manuscript. All authors have approved the final version of the manuscript.

Notes

The authors declare no competing financial interest.

■ ABBREVIATIONS

ACQ, aggregation-induced quenching; AIE, aggregation-induced emission; ALP, alkaline phosphatase; ALT, alanine aminotransferase; AST, aspartate aminotransferase; BSA, bovine serum albumin; CMC, critical micelle concentration; CLSM, confocal laser scanning microscope; DCK, deoxycytidine kinase; DLC, drug loading content; DNA, DNA; EPR, enhanced permeability and retention; FBS, fetal bovine serum; GEM, gemcitabine; GSH, glutathione; H&E, hematoxylin and eosin; HPLC, high-performance liquid chromatography; HAS, human serum albumin; IHC, immunohistochemical; MRI, magnetic resonance imaging; NIR, near-infrared; NMR, nuclear magnetic resonance; PBS, phosphate-buffered saline; PEG, polyethylene glycol; PEITC, phenyl isothiocyanate; ROS, reactive oxygen species; SNR, signal-to-noise ratio; TEM, transmission electron microscopy

■ REFERENCES

(1) Siegel, R. L.; Miller, K. D.; Fuchs, H. E.; Jemal, A. Cancer statistics, 2022. *Ca-Cancer J. Clin.* **2022**, 72, 7−33.

(2) Weingart, S. N.; Zhang, L.; Sweeney, M.; Hassett, M. Chemotherapy medication errors. *Lancet Oncol.* **2018**, 19, 191−199.

(3) Livingston, E. H.; Li, H. C. Breast Cancer Surgery: Less Is More. *J. Am. Med. Assoc.* **2017**, *318*, 909−911.

(4) Catton, C.; Lukka, H. The evolution of fractionated prostate cancer radiotherapy. *Lancet* **2019**, *394*, 361−362.

(5) Ke, X.; Shen, L. Molecular targeted therapy of cancer: The progress and future prospect. *Front. Lab. Med.* **2017**, *1*, 69−75.

(6) Maeda, H.; Nakamura, H.; Fang, J. The EPR effect for macromolecular drug delivery to solid tumors: Improvement of tumor uptake, lowering of systemic toxicity, and distinct tumor imaging in vivo. *Adv. Drug Delivery Rev.* **2013**, *65*, 71−79.

(7) Zhou, Y.; Dong, H.; Gu, Z.; Yang, S.; Ouyang, M.; Qing, Z.; Ma, X.; Hu, S.; Li, J.; Yang, R. S. Self-Immolative Dye-Doped Polymeric Probe for Precisely Imaging Hydroxyl Radicals by Avoiding Leakage. *Anal. Chem.* **2021**, *93*, 12944−12953.

(8) Xue, Y.; Bai, H.; Peng, B.; Fang, B.; Baell, J.; Li, L.; Huang, W.; Voelcker, N. H. Stimulus-cleavable chemistry in the field of controlled drug delivery. *Chem. Soc. Rev.* **2021**, *50*, 4872−4931.

(9) Guo, X.; Wang, L.; Duval, K.; Fan, J.; Zhou, S.; Chen, Z. Dimeric Drug Polymeric Micelles with Acid-Active Tumor Targeting and FRET-Traceable Drug Release. *Adv. Mater.* **2018**, *30*, No. 1705436.

(10) Grubbs, R. B.; Sun, Z. Shape-changing polymer assemblies. *Chem. Soc. Rev.* **2013**, *42*, 7436−7445.

(11) Karimi, M.; Ghasemi, A.; Sahandi Zangabad, P.; Rahighi, R.; Moosavi Basri, S. M.; Mirshekari, H.; Amiri, M.; Shafaei Pishabad, Z.; Aslani, A.; Bozorgomid, M.; Ghosh, D.; Beyzavi, A.; Vaseghi, A.; Aref, A. R.; Haghani, L.; Bahrami, S.; Hamblin, M. R. Smart micro/nanoparticles in stimulus-responsive drug/gene delivery systems. *Chem. Soc. Rev.* **2016**, *45*, 1457−1501.

(12) Yu, X.; Qi, S.; Cao, F.; Yang, K.; Li, H.; Peng, K.; Liu, Z.; Bai, B.; Buljan, M.; Chen, X.; Yu, G. Fabrication of An Immunostimulatory Supramolecular Nanomedicine for Potent Cancer Chemo-immunotherapy. *JACS Au* **2023**, *3*, 3181−3193.

(13) Van Der Vlies, A. J.; Xu, J.; Ghasemi, M.; Bator, C.; Bell, A.; Rosoff-Verbit, B.; Liu, B.; Gomez, E. D.; Hasegawa, U. Thioether-Based Polymeric Micelles with Fine-Tuned Oxidation Sensitivities for Chemotherapeutic Drug Delivery. *Biomacromolecules* **2022**, *23*, 77−88.

(14) Zhang, H. J.; Zhao, X.; Chen, L. J.; Yang, C. X.; Yan, X. P. pH-Driven Targeting Nanoprobe with Dual-Responsive Drug Release for Persistent Luminescence Imaging and Chemotherapy of Tumor. *Anal. Chem.* **2020**, *92*, 1179−1188.

(15) Gui, R.; Wan, A.; Zhang, Y.; Li, H.; Zhao, T. Ratiometric and Time-Resolved Fluorimetry from Quantum Dots Featuring Drug Carriers for Real-Time Monitoring of Drug Release in Situ. *Anal. Chem.* **2014**, *86*, 5211−5214.

(16) Yi, X.; Hu, J. J.; Dai, J.; Lou, X.; Zhao, Z.; Xia, F.; Tang, B. Z. Self-Guiding Polymeric Prodrug Micelles with Two Aggregation-Induced Emission Photosensitizers for Enhanced Chemo-Photodynamic Therapy. *ACS Nano* **2021**, *15*, 3026−3037.

(17) Zhang, L.; Wang, Y.; Zhang, X.; Wei, X.; Xiong, X.; Zhou, S. Enzyme and Redox Dual-Triggered Intracellular Release from Actively Targeted Polymeric Micelles. *ACS Appl. Mater. Interfaces* **2017**, *9*, 3388−3399.

(18) Wan, D.; Zhu, Q.; Zhang, J.; Chen, X.; Li, F.; Liu, Y.; Pan, J. Intracellular and extracellular enzymatic responsive micelle for intelligent therapy of cancer. *Nano Res.* **2022**, *16*, 2851−2858.

(19) Hao, Y.; Song, K.; Tan, X.; Ren, L.; Guo, X.; Zhou, C.; Li, H.; Wen, J.; Meng, Y.; Lin, M.; Zhang, Y.; Huang, H.; Wang, L.; Zheng, W. Reactive Oxygen Species-Responsive Polypeptide Drug Delivery System Targeted Activated Hepatic Stellate Cells to Ameliorate Liver Fibrosis. *ACS Nano* **2022**, *16*, 20739−20757.

(20) Ma, B.; Xu, H.; Zhuang, W.; Wang, Y.; Li, G.; Wang, Y. Reactive Oxygen Species Responsive Theranostic Nanoplatform for Two-Photon Aggregation-Induced Emission Imaging and Therapy of Acute and Chronic Inflammation. *ACS Nano* **2020**, *14*, 5862−5873.

(21) Fan, Y.; Chen, L.; Zheng, Y.; Li, A.; Lin, H.; Gao, J. Nanoparticle-Based Activatable MRI Probes for Disease Imaging and Monitoring. *Chem. Biomed. Imaging* **2023**, *1*, 192−204.

(22) Ling, S.; Yang, X.; Li, C.; Zhang, Y.; Yang, H.; Chen, G.; Wang, Q. Tumor Microenvironment-Activated NIR-II Nanotheranostic System for Precise Diagnosis and Treatment of Peritoneal Metastasis. *Angew. Chem., Int. Ed.* **2020**, *59*, 7219−7223.

(23) Li, C.; Li, W.; Liu, H.; Zhang, Y.; Chen, G.; Li, Z.; Wang, Q. An Activatable NIR-II Nanoprobe for In Vivo Early Real-Time Diagnosis of Traumatic Brain Injury. *Angew. Chem., Int. Ed.* **2020**, *59*, 247−252.

(24) Zhan, Y.; Ling, S.; Huang, H.; Zhang, Y.; Chen, G.; Huang, S.; Li, C.; Guo, W.; Wang, Q. Rapid Unperturbed-Tissue Analysis for Intraoperative Cancer Diagnosis Using an Enzyme-Activated NIR-II Nanoprobe. *Angew. Chem., Int. Ed.* **2021**, *60*, 2637−2642.

(25) Cheng, X.; Xu, H. D.; Ran, H. H.; Liang, G.; Wu, F. G. Glutathione-Depleting Nanomedicines for Synergistic Cancer Therapy. *ACS Nano* **2021**, *15*, 8039−8068.

(26) Wang, X. B.; Li, H. J.; Liu, C.; Hu, Y. X.; Li, M. C.; Wu, Y. C. Simple Turn-On Fluorescent Sensor for Discriminating Cys/Hcy and GSH from Different Fluorescent Signals. *Anal. Chem.* **2021**, *93*, 2244−2253.

(27) Zhao, Z.; Zhang, Y.; Wu, M.; Yan, C.; Guo, Z. A Reversible Dual-Channel Near-Infrared Flavonoid Probe for in Vivo Tracking Glutathione Dynamics in Living Mice. *Chem. Biomed. Imaging* **2023**, *1*, 620−627.

(28) Liu, K.; Kang, B.; Luo, X.; Yang, Z.; Sun, C.; Li, A.; Fan, Y.; Chen, X.; Gao, J.; Lin, H. Redox-Activated Contrast-Enhanced T_1-Weighted Imaging Visualizes Glutathione-Mediated Biotransformation Dynamics in the Liver. *ACS Nano* **2021**, *15*, 17831−17841.

(29) Ouyang, X.; Jia, N.; Luo, J.; Li, L.; Xue, J.; Bu, H.; Xie, G.; Wan, Y. DNA Nanoribbon-Assisted Intracellular Biosynthesis of Fluorescent Gold Nanoclusters for Cancer Cell Imaging. *JACS Au* **2023**, *3*, 2566−2577.

(30) Zou, Y.; Li, M.; Xing, Y.; Duan, T.; Zhou, X.; Yu, F. Bioimaging of Glutathione with a Two-Photon Fluorescent Probe and Its Potential Application for Surgery Guide in Laryngeal Cancer. *ACS Sens.* **2020**, *5*, 242−249.

(31) Liu, H.; Song, W.; Zhang, S.; Chan, K. S.; Guo, Z.; Shen, Z. A ratiometric fluorescent probe for real-time monitoring of intracellular glutathione fluctuations in response to cisplatin. *Chem. Sci.* **2020**, *11*, 8495−8501.

(32) Zhao, Z.; Zhang, H.; Lam, J. W. Y.; Tang, B. Z. Aggregation-Induced Emission: New Vistas at the Aggregate Level. *Angew. Chem., Int. Ed.* **2020**, *59*, 9888−9907.

(33) Li, Z.; Ji, X.; Xie, H.; Tang, B. Z. Aggregation-Induced Emission-Active Gels: Fabrications, Functions, and Applications. *Adv. Mater.* **2021**, *33*, No. 2100021.

(34) Ghosh, A. K.; Khan, A. H.; Das, P. K. Naphthalimide-Based AIEgens for Sensing Protein Disulfide Isomerase through Thiol−Disulfide Redox Exchange. *Anal. Chem.* **2023**, *95*, 13638−13648.

(35) Xu, C.; Wu, T.; Duan, L.; Zhou, Y. A naphthalimide-derived hypochlorite fluorescent probe from ACQ to AIE effect transformation. *Chem. Commun.* **2021**, *57*, 11366−11369.

(36) Kim, Y. K.; Lee, J. E.; Ryplida, B.; Choi, C. A.; Mazrad, Z. A. I.; Lee, G.; Lee, S.; In, I.; Jeong, J. H.; Park, S. Y. Redox-responsive FRET-based polymer dot with BODIPY for fluorescence imaging-guided chemotherapy of tumor. *Eur. J. Pharm. Biopharm.* **2018**, *132*, 200−210.

(37) Terreno, E.; Castelli, D. D.; Viale, A.; Aime, S. Challenges for molecular magnetic resonance imaging. *Chem. Rev.* **2010**, *110*, 3019−3042.

(38) Feinberg, D. A.; Beckett, A. J. S.; Vu, A. T.; Stockmann, J.; Huber, L.; Ma, S.; Ahn, S.; Setsompop, K.; Cao, X.; Park, S. Next-generation MRI scanner designed for ultra-high-resolution human brain imaging at 7 T. *Nat. Methods* **2023**, *20*, 2048−2057.

(39) Liu, W.; Yin, S.; Hu, Y.; Deng, T.; Li, J. Microemulsion-Confined Biomineralization of PEGylated Ultrasmall Fe_3O_4 Nanocrystals for T_2-T_1 Switchable MRI of Tumors. *Anal. Chem.* **2021**, *93*, 14223−14230.

(40) Zhou, Z.; Yang, L.; Gao, J.; Chen, X. Structure-Relaxivity Relationships of Magnetic Nanoparticles for Magnetic Resonance Imaging. *Adv. Mater.* **2019**, *31*, No. 1804567.

(41) Chen, J.; Lanza, G. M.; Wickline, S. A. Quantitative magnetic resonance fluorine imaging: today and tomorrow. *Wiley Interdiscip. Rev.: Nanomed. Nanobiotechnol.* **2010**, *2*, 431−440.

(42) Knight, J. C.; Edwards, P. G.; Paisey, S. J. Fluorinated contrast agents for magnetic resonance imaging; a review of recent developments. *RSC Adv.* **2011**, *1*, 1415−1425.

(43) Zhang, C.; Moonshi, S. S.; Wang, W.; Ta, H. T.; Han, Y.; Han, F. Y.; Peng, H.; Král, P.; Rolfe, B. E.; Gooding, J. J.; Gaus, K.; Whittaker, A. K. High F-Content Perfluoropolyether-Based Nanoparticles for Targeted Detection of Breast Cancer by ^{19}F Magnetic Resonance and Optical Imaging. *ACS Nano* **2018**, *12*, 9162−9176.

(44) Cao, Y.; Zhou, X.; Liu, X.; Yang, M.; Liu, W.; Han, D. High-Sensitivity, Low-Field ^{19}F-MRI Approach Using High Manganese Ferrite Concentrations. *Anal. Chem.* **2023**, *95*, 10572−10579.

(45) Ikari, M.; Yagi, H.; Kasai, T.; Inomata, K.; Ito, M.; Higuchi, K.; Matsuda, N.; Ito, Y.; Kigawa, T. Direct Observation of Membrane-Associated H-Ras in the Native Cellular Environment by In-Cell ^{19}F-NMR Spectroscopy. *JACS Au* **2023**, *3*, 1658−1669.

(46) Tian, M.; Liu, X. Y.; He, H.; Ma, X. Z.; Liang, C.; Liu, Y.; Jiang, F. L. Real-Time Imaging of Intracellular Glutathione Levels Based on a Ratiometric Fluorescent Probe with Extremely Fast Response. *Anal. Chem.* **2020**, *92*, 10068−10075.

(47) Ge, J.; Cai, R.; Chen, X.; Wu, Q.; Zhang, L.; Jiang, Y.; Cui, C.; Wan, S.; Tan, W. Facile approach to prepare HSA-templated MnO_2 nanosheets as oxidase mimic for colorimetric detection of glutathione. *Talanta* **2019**, *195*, 40−45.

(48) Cui, C. Y.; Li, B.; Cheng, D.; Li, X. Y.; Chen, J. L.; Chen, Y. T.; Su, X. C. Simultaneous Quantification of Biothiols and Deciphering Diverse GSH Stability in Different Live Cells by ^{19}F-Tag. *Anal. Chem.* **2022**, *94*, 901−908.

(49) Zhou, W.; Yin, B. C.; Ye, B. C. Highly sensitive surface-enhanced Raman scattering detection of hexavalent chromium based on hollow sea urchin-like TiO_2@Ag nanoparticle substrate. *Biosens. Bioelectron.* **2017**, *87*, 187−194.

(50) Peng, H. P.; Jian, M. L.; Huang, Z. N.; Wang, W. J.; Deng, H. H.; Wu, W. H.; Liu, A. L.; Xia, X. H.; Chen, W. Facile electrochemiluminescence sensing platform based on high-quantum-yield gold nanocluster probe for ultrasensitive glutathione detection. *Biosens. Bioelectron.* **2018**, *105*, 71−76.

(51) Giustarini, D.; Dalle-Donne, I.; Colombo, R.; Milzani, A.; Rossi, R. An improved HPLC measurement for GSH and GSSG in human blood. *Free Radicals Biol. Med.* **2003**, *35*, 1365−1372.

(52) Chen, S.; Xiao, L.; Li, Y.; Qiu, M.; Yuan, Y.; Zhou, R.; Li, C.; Zhang, L.; Jiang, Z. X.; Liu, M.; Zhou, X. In Vivo Nitroreductase Imaging via Fluorescence and Chemical Shift Dependent ^{19}F NMR. *Angew. Chem., Int. Ed.* **2022**, *61*, No. e202213495, DOI: 10.1002/ange.202213495.

(53) Lin, C. T.; Lin, I. C.; Sung, S. Y.; Su, Y. L.; Huang, Y. F.; Chiang, C. S.; Hu, S. H. Dual-Targeted Photopenetrative Delivery of Multiple Micelles/Hydrophobic Drugs by a Nanopea for Enhanced Tumor Therapy. *Adv. Funct. Mater.* **2016**, *26*, 4169−4179.

(54) Zhou, H.; Fan, Z.; Li, P. Y.; Deng, J.; Arhontoulis, D. C.; Li, C. Y.; Bowne, W. B.; Cheng, H. Dense and Dynamic Polyethylene Glycol Shells Cloak Nanoparticles from Uptake by Liver Endothelial Cells for Long Blood Circulation. *ACS Nano* **2018**, *12*, 10130−10141.

(55) Liu, R.; Tang, J.; Xu, Y.; Zhou, Y.; Dai, Z. Nano-sized Indocyanine Green J-aggregate as a One-component Theranostic Agent. *Nanotheranostics* **2017**, *1*, 430−439.